On the Impact of Nonuniform Phase Distributions Across the Beamwidth and Bandwidth of Antennas for SAR Imaging

Alicia Flórez Berdasco, *Graduate Student Member, IEEE*, Jaime Laviada, María Elena de Cos Gómez, *Member, IEEE*, and Fernando Las-Heras, *Senior Member, IEEE*

***Abstract*— The synthetic aperture radar (SAR) imaging relies on the coherent sum of the received signals. Consequently, phase shifts along the beamwidth and bandwidth of the antenna radiation pattern can have a relevant impact on the final image. Previous studies have focused on other sources of image quality degradation, such as antenna mispositioning, frequency uncertainty, or antenna gain pattern effect. This article demonstrates that the phase of the antenna radiation pattern plays a critical role in the quality of the computed electromagnetic images. For this purpose, three different situations have been analyzed: 1) the phase shift changes across the angular range; 2) the nonlinear phase displacement across the working frequency band; and 3) antenna phase center drift across the bandwidth. Systematic simulations have been carried out modeling these phase shifts for different antennas and enabling to establish rules of thumb for the thresholds in all of the previous cases.**

***Index Terms*— Image distortion, image quality degradation, imaging, millimeter-wave (mmWave) radar, mmWave imaging, synthetic aperture radar (SAR).**

I. Introduction

RADAR technology was initially designed to estimate the distance to a given target not only enabling the detection of some visible but also hidden objects, even in adverse weather conditions and in darkness [1]. The angular resolution was limited by the aperture of the radar, which led to the use of synthetic aperture radar (SAR) that leverages the information at multiple positions to create high resolution images [2]. Later, the advent of millimeter-wave (mmWave) technology, motivated by high bandwidth communications and advanced driver assistance systems (ADAS), has led to a reduction in the cost and evolution of mmWave radars yielding compact and affordable modules [3]. As a result, nowadays, there are a large number of applications based on mmWave radar technology, such as nondestructive testing (NDT) [4], [5], [6], [7], security [8], [9], medical imaging [10], [11], and among others.

In order to implement SAR techniques, after collecting the reflected data for different positions over the virtual aperture, an imaging algorithm is used. The straightforward implementation is by means of delay-and-sum algorithms but range-migration techniques are also available for an efficient implementation [12], [13]. These algorithms coherently add all the reflected signals, for each frequency and position, assuming a perfect spherical wavefront, which greatly improves the noise-to-signal ratio. However, the quality of the images is degraded if the ideal radiation pattern is not satisfied.

In addition, the image quality can also be degraded by other sources of errors. Some of them, such as the influence of antenna mispositioning, have been recently analyzed [14], [15]. The aforementioned works distinguished two types of positioning errors. On the one hand, the so-called lateral positioning errors, which are displacements in the position of the antenna in the measurement plane. On the other hand, those are referred to as height errors, which occur on the axis between the measurement plane and the target location plane. All these kind of positioning errors causes an incorrect phase compensation in the SAR algorithm, which results in the degradation of the quality and image distortion. However, previous studies demonstrated that height errors lead to further significant degradation of the image than lateral ones, which can be usually disregarded. For a concrete distance to the target, the spatial resolution worsens as the height error increases. In addition, the error in the original location of the target and the image error increases as the maximum height position error raises.

In SAR imaging systems, the another effect that has been studied, is the impact caused by frequency uncertainty, which is reviewed in [16] and [17]. This work focuses on frequency uncertainty produced by system instrumentation, which is defined as the difference between the real frequency at which the echo signal is recorded and that used to generate the image. Image degradation raises with both frequency uncertainty and target remoteness, so that distortion is more evident for distant targets as the frequency increases. However, in the case of near-field SAR, where the target is very close to the synthetic aperture, high levels of frequency uncertainty can

Manuscript received 23 January 2024; revised 19 May 2024; accepted 23 May 2024. Date of publication 15 July 2024; date of current version 26 July 2024. This work was supported in part by the Ministerio de Ciencia e Innovación of Spain under the Formación Personal Investigador (FPI) Grant MCIU-20-PRE2019-089912 and under Project META-IMAGER PID2021-122697OBI00, and in part by the Gobierno del Principado de Asturias under Project AYUD-2021-51706. The Associate Editor coordinating the review process was Dr. Matthew Dvorsky. *(Corresponding author: Alicia Flórez Berdasco.)*

The authors are with the Department of Electrical Engineering, University of Oviedo, 33203 Gijón, Spain (e-mail: florezalicia@uniovi.es; laviadajaime@uniovi.es; flasheras@uniovi.es).

Digital Object Identifier 10.1109/TIM.2024.3428623

be tolerated before image quality degradation and distortion become noticeable [17].

The influence of the nonuniform amplitude of the radiation pattern of an antenna in image quality has been analyzed in [18]. The analysis has been done for both near-field and far-field detection by analyzing the range and cross-range resolutions. In this work, the amplitude of the full radiation pattern is used, and the results are compared with those of previous studies, in which only the half-power beamwidth (HPBW) was taken into account. The work concludes that the complete antenna gain radiation pattern plays a fundamental role for both, range and cross-range resolution, especially in the case of near-field detection, in which the synthetic aperture length is considerably larger than the depth distance.

Despite the previous analysis, the effect of nonuniform phase along the beamwidth and bandwidth of the radiation pattern of the antenna has been usually ignored. A recent work [19] proposes an elaborated processing technique to accurately compensate for the phase effects, but it requires a fully vector characterization (amplitude and phase) of the antenna and a more complex imaging algorithm. In contrast to the aforementioned reference, this work aims to analyze the influence of oscillating phase shifts in image quality by studying the effects through three different scenarios, namely, linear phase shift across space, linear or oscillating frequency shift, and phase center shift across the bandwidth. Modeling through linear phase shifts and oscillating behaviors is considered since they are found illustrative and enable to estimate reasonable rules of thumb, though more arbitrary phase changes can take place. Although other system parameters (e.g., phase noise) may affect the phase distribution, their consideration is out of the scope of this study, which focuses only on the analysis of the phase effects of the antenna radiation pattern on electromagnetic imaging.

The nonuniform phase effects have been analyzed by simulating a monostatic system, which is moved through a plane to implement the synthetic aperture radar techniques. Concretely, a stepped-frequency continuous-wave radar is considered throughout the whole work.

This article is organized as follows. First, the main concerns about the typical SAR imaging algorithms used to generate the electromagnetic images are explained. Later, a brief introduction to the three-phase shifts considered in this study along with their respective main issues are presented. Then, the simulation setup for each situation is described, and the results are presented with a discussion of the outcomes. Finally, the conclusion is drawn.

II. Impact of Phase Shifts in Image Quality

In the context of SAR imaging, images are generated through a flexible *sum-and-delay* algorithm [2], which assumes that the transmitted wave is an ideal spherical wavefront signal

$$S_{\text{tx}}(m,n) = \frac{1}{|\vec{r}\,' - \vec{r}_n|} e^{-jk_m|\vec{r}\,'-\vec{r}_n|} \tag{1}$$

where k_m refers to the wavenumber at the mth frequency, $\vec{r}_n$ stands for the nth measured position, and $\vec{r}\,'$ represents the position of the target (see Fig. 1). It is convenient to note that the amplitude decay factor $\frac{1}{|\vec{r}\,'-\vec{r}_n|}$ is usually neglected in (1) as it does not have a relevant contribution to the imaging algorithm. In the case of a monostatic acquisition, in which the receiver antenna is the same as the transmitter one, the received signal captured by the system corresponds to the echo produced by a target, so that the recorded contribution becomes a delayed version of the transmitted one after being reflected

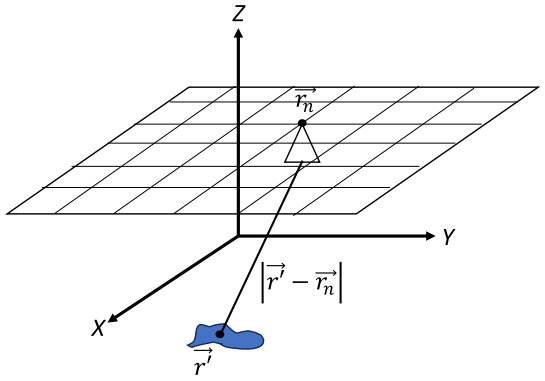

Fig. 1. Schematic for conventional monostatic SAR measurements.

$$S_{\text{rx}}(m,n) = \int_V \rho(\vec{r}\,') e^{-j2k_m|\vec{r}\,'-\vec{r}_n|} dV \tag{2}$$

where ρ indicates the reflectivity of the target and V is a volume including the target. This received signal is processed to estimate the reflectivity at each point $\vec{r}\,'$, yielding the final image. For this purpose, the delay is compensated by coherently adding the contributions at different positions and frequencies behaving as a matched filter

$$\hat{\rho}(\vec{r}\,') = \sum_{m=1}^{M}\sum_{n=1}^{N} S_{\text{rx}}(m,n) \cdot e^{j2k_m|\vec{r}\,'-\vec{r}_n|}. \tag{3}$$

The previous equations ideally require a uniform spherical wavefront without angular or spatial changes in terms of amplitude and phase, being the latter a cornerstone to guarantee the coherent sum. Although some recent techniques [20] are able to compensate nonideal effects, their mitigation comes at the expense of avoiding the use of efficient range-migration techniques to implement (3).

This work aims to explore the effect of the nonuniform phase along the beamwidth and bandwidth of the antenna in the electromagnetic images. For this purpose, the main three different causes have been identified, and their corresponding impact explored below.

A. Nonuniform Phase Across the Beamwidth

For real-world antennas, the phase radiation pattern of the antenna along its beamwidth is not constant. Consequently, the basic algorithm shown in (3) cannot completely compensate the phase to create a coherent sum. Therefore, the quality of the image depicting the reflectivity is degraded. In order to illustrate this effect, let us consider the patch antenna presented in [24], which was designed on RO3003 ($\varepsilon_r = 3.0$,

$\tan\delta = 0.0013$, and $h = 0.762$ mm), and it is exhibited in Fig. 2(a). Fig. 2(b) and (c) depicts the magnitude and phase of the co-polar (CP) and cross-polar (XP) components for the E- and H-plane cuts of the radiation pattern. However, the XP component will be ignored due to its low relevance. This antenna shows a moderate phase shift along the center of the beamwidth, as shown in Fig. 2(b) and (c). If this antenna is used to create a SAR image, as shown in Fig. 2(d), it can be observed that the target, scissors in this case, has suffered a displacement with respect to its original position, which has been highlighted in red in the image. That image was generated at the frequency band of 24.05–24.25 GHz using a grid of point over an area of 20 × 20 cm at 5 cm from the target. The distance between points was $\lambda/4$ corresponding λ to the maximum working frequency.

Thus, it is clear that this kind of phase shift can have a relevant impact on the final image, hindering the coherent combination of the waves. In order to understand the effect exhibited in Fig. 2(d), let us express (3) by means of range-migration techniques using the Fourier transform [12]

$$\hat{\rho}\left(\overrightarrow{r}\right) = \mathrm{FT}_{3\mathrm{D}}^{-1}\left[\mathrm{FT}_{2\mathrm{D}}\left[S_{\mathrm{rx}}\left(\overrightarrow{r}_n, k_m\right)\right] \cdot e^{-jk_{m,z}\left|\overrightarrow{r}' - \overrightarrow{r}_n\right|}\right] \quad (4)$$

where $k_{m,z} = (k_m^2 - k_x^2 - k_y^2)^{1/2}$, being k_x and k_y, the spectral coordinates corresponding to x and y. Therefore, according to (4), if the phase of the antenna radiation pattern shows a linear phase shift, some displacement of the target with respect to its initial position can take place. This kind of phase shift as well as more arbitrary ones can result in contributions not adding coherently, resulting in image degradation.

B. Linear or Oscillating Phase Shift Across Frequency

In addition to changes along the beamwidth, antennas are also not expected to have a constant phase along their bandwidth. In general, a predominant linear phase shift is observed as a consequence of the feeding network. Consequently, antennas exhibit a linear negative slope phase term for the CP component along frequency (as already mentioned, due to its low relevance, the XP component will be ignored), which can be expressed as e^{-jkL}, being k the wavenumber [see Fig. 3(a)]. The parameter L of the linear phase term is usually estimated during an initial calibration stage and removed by multiplying by the opposite phase [22], so that a constant phase over the working frequency band is expected after calibration. However, in practice, especially in wideband antennas, the phase of the radiation pattern suffers some ripple, which is not fully compensated by the previous linear calibration.

It is important to note that this effect has no impact if the image is obtained at a single frequency. In fact, according to (3), the final image can be expressed as follows:

$$\hat{\rho}\left(\overrightarrow{r}\right) = \sum_{m=1}^{M} \hat{\rho}_m\left(\overrightarrow{r}\right) e^{j\vartheta_m} \quad (5)$$

where $\hat{\rho}_m(\overrightarrow{r})$ is the image obtained using only the mth frequency, and ϑ_m is the residual phase shift after calibration at the mth frequency. Thus, the linear combination of the single-frequency electromagnetic images can result in contributions that are added in-phase and others in counterphase. On the one hand, the lateral resolution does not depend on the frequency bandwidth [12], and therefore, the addition of noncoherently single-frequency images will result in a reduction of the dynamic range for images parallel to the acquisition plane. In addition, the resolution in the range is proportional to the available bandwidth, and therefore, it is expected to be reduced if different single-frequency images are not in-phase.

C. Phase Center Shift Across Frequency

Finally, a critical factor to consider in order to obtain the high quality images is the potential shift of the antenna phase center. The antenna phase center corresponds to the position from which the theoretical spherical wavefront emanates. In general, this phase center does not have to coincide with the physical center of the antenna. Moreover, it can vary depending on the frequency, moving in any direction. Moderate lateral displacements (and their corresponding errors) are not expected to have a relevant impact [14], [15]. In addition, antenna symmetries can be exploited to avoid phase center lateral movements. Nevertheless, height changes (with respect to the synthetic aperture) of the phase center are difficult to control. Since height errors have a key impact on the image quality [14], [15], they should be minimized. Hence, it is relevant to know the location of the phase center and the effects that its displacement can produce in electromagnetic images.

The movement of the phase center is especially noteworthy in wideband antennas, as it can be appreciated in Fig. 4, which shows the phase center offset behavior of a Vivaldi wideband antenna. In that antenna, linear and oscillating regions can be distinguished for the phase center displacement.

III. Impact of Nonideal Phase Distribution

In order to analyze the impact of the nonuniform phase in electromagnetic imaging, a monostatic system has been simulated in the frequency band of 22–26 GHz. Simulations have been chosen instead of measurements as they enable us to control each cause, and the subsequent effect, independently. The spatial sweep has been performed along a plane of 20 × 20 cm at a distance of 15 cm from the target. The sampling step has been set to $\lambda/4$ (λ at the highest frequency) to meet the Nyquist sampling theorem avoiding additional artifacts. The SAR system configuration parameters are summarized in Table I.

A point-like target is used in this work to ease the comparison and analysis of the results [14], [15]. In this case, the point-like target is modeled by means of an icosahedron with a size ten times smaller than the wavelength. Thus, the obtained electromagnetic images are equivalent to the so-called point spread function (PSF).

In order to find a trade-off between simulation speed and model accuracy, a hybrid approach mixing realistic radiation patterns and physical optics (PO) was adopted. The system has been simulated following the flowchart shown in Fig. 5. First, several antennas, which were previously designed using the 3-D High-Frequency Simulation Software HFSS

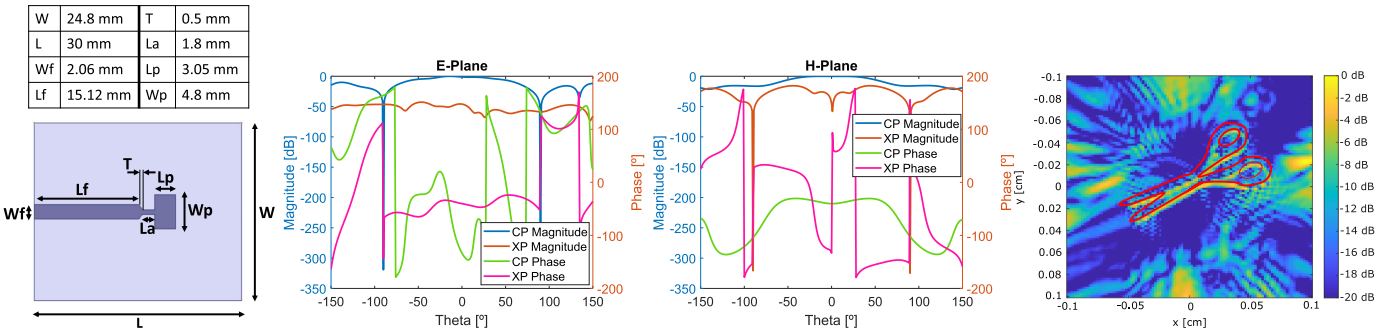

Fig. 2. Effects of linear phase offset along the beamwidth of the antenna. (a) Antenna geometry, (b) E-plane (co-polar CP and crosspolar XP), (c) H-plane, and (d) reflectivity.

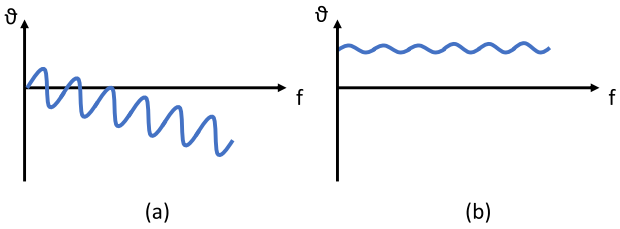

Fig. 3. Schematic of the phase of the radiation pattern. (a) Phase shift across frequency before linear calibration. (b) Phase shift across frequency after linear calibration.

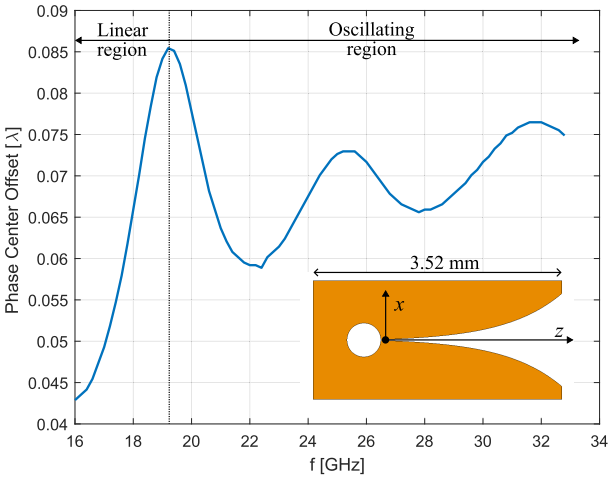

Fig. 4. Phase center offset across the z-axis for a wideband Vivaldi antenna.

TABLE I
SAR SYSTEM CONFIGURATION

Center frequency [GHz]	24
Bandwidth [GHz]	4
Number of frequencies	40
Synthetic aperture measurement plane size [cm]	20×20
Sampling Step [m]	$\lambda_m/4$
Distant to the target [cm]	15

of Ansys [23], are simulated to obtain the far-field antenna radiation pattern. Then, the radiation pattern is imported in MATLAB to perform the SAR acquisition and imaging. The SAR acquisition is implemented by generating the required acquisition grid, passing this configuration to FEKO, and implementing the PO solver which carries out the electromagnetic simulation by modeling the propagation of the

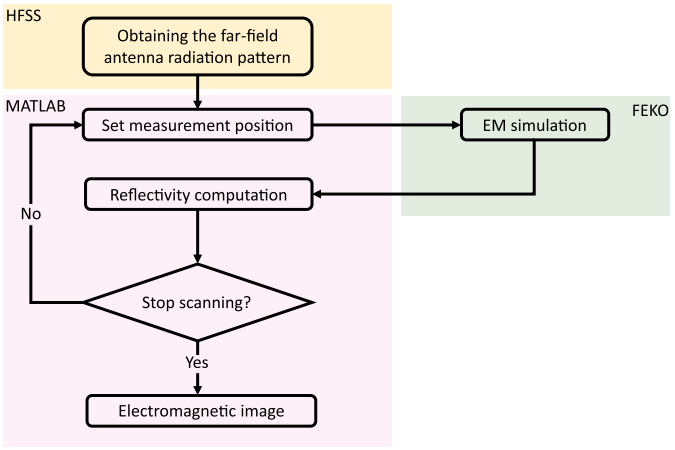

Fig. 5. Simulation flowchart.

transmitted and reflected signals considering the imported radiation patterns. Finally, the reflected signal is returned to MATLAB to compute the reflectivity by means of (3) and continue scanning if there are pending measurement positions, otherwise, provide the calculated electromagnetic image.

Three different antennas are considered in order to compare the effects throughout different types of radiation patterns, whose phase will be conveniently modified to model the effects described in Section II. A patch antenna with a quasi-omnidirectional radiation pattern [24] as well as a two-element patch-array antenna [25], which includes a high impedance surface (HIS) to improve its radiation properties, are used as models of low and medium gain antennas. These antennas have a directivity of 6.8 and 9.2 dB, respectively. The dataset corresponding to the radiation patterns of the patch and array antennas can be found in [26]. In order to provide a comparison with a higher directivity antenna, a horn antenna modeled with an ideal radiation pattern represented as $\cos^q(\theta)$, with $q = 8$, and no backward radiation (directivity of 15 dB) is also studied.

A. Linear Phase Shift Across Space

In order to analyze the effect that causes the nonuniformity of the phase in the antenna's radiation pattern, different phase shifts have been explored. In particular, linear phase shifts have been considered. Since introducing the phase shift through the

TABLE II
DISPLACEMENT OF THE TARGET WITH RESPECT TO ITS ORIGINAL POSITION IN THE y-AXIS FOR DIFFERENT PHASE OFFSETS

Slope, a	0	2	4	6	8	10	12	14
Target displacement for the patch antenna [λ]	0	0.86	1.48	2.09	2.87	3.48	4.17	4.78
Target displacement for the array antenna [λ]	0	0.70	1.39	2.09	2.87	3.48	4.17	4.87
Target displacement for the horn antenna [λ]	0	0.70	1.39	2	2.87	3.57	4.17	4.96

spherical coordinates θ or ϕ would result in very unrealistic phase distributions, even in the beamwidth, it was introduced through the u–v coordinates instead, as it results in more natural distributions. The u–v coordinates are often used to represent radiation patterns in a 2-D representation. They can be obtained from spherical coordinates as follows:

$$u = \sin(\theta) \cdot \cos(\varphi) \tag{6}$$

$$v = \sin(\theta) \cdot \sin(\varphi). \tag{7}$$

Specifically, the linear phase shift has been applied to the E-plane pattern by modifying the v-coordinate as follows:

$$E(u, v) = E(u, v)e^{(jav)} \tag{8}$$

where E refers to the electromagnetic field and a stands for the slope that modifies the linear phase offset.

Simulations with different linear phase shifts have been performed. Fig. 6 shows some of the PSFs obtained for the patch antenna. As expected, it can be concluded that as the slope of the nonuniform phase increases, the displacement of the target from its original position (which has been pointed out in red in the images) becomes greater. Moreover, the blurring suffered around the target is greater as the slope rises. This kind of electromagnetic images has been obtained for each antenna and slope value. However, only part of the representative ones are shown here. It is worth noting that this phase shift seems to be responsible for the displacement shown in the aforementioned example using an unmodified phase, which is illustrated in Fig. 2. Electromagnetic images without phase shift ($a = 0$) for the array and horn antenna are shown in Fig. 7 as a reference. Fig. 8 represents the displacement suffered by the target with respect to its original position against the slope a. The displacement of the target increases almost linearly with the phase slope value. The results are similar for all the radiation patterns under evaluation, as it can be observed from Table II. Therefore, in this case of analysis, the directivity of the antenna does not have a significant impact on the electromagnetic image (except for the sidelobe level around the target due to the amplitude taper), and the main contribution to the target displacement is produced by the phase shift.

Table III gathers the sidelobe level of the reflectivity (following the analogy with the secondary lobes of an antenna radiation pattern) for each phase shift. As expected, the

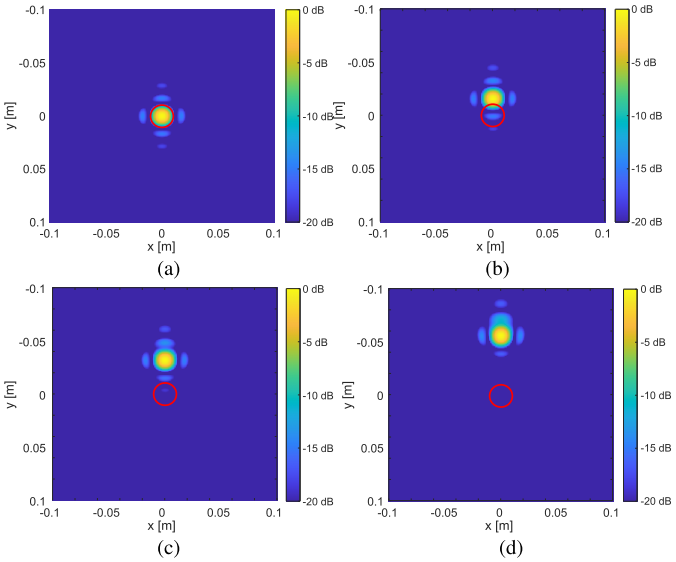

Fig. 6. Electromagnetic images of the patch antenna for different slope values. (a) $a = 0$, (b) $a = 4$, (c) $a = 8$, and (d) $a = 14$.

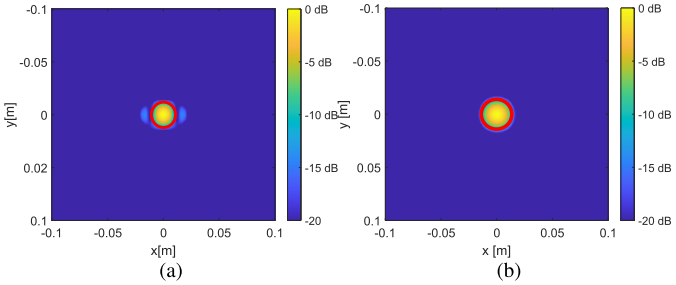

Fig. 7. Electromagnetic images with $a = 0$. (a) Array antenna. (b) Horn antenna.

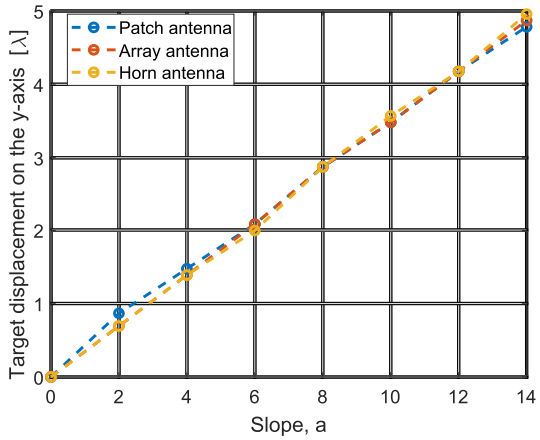

Fig. 8. Displacement of the target on the y-axis versus slope, a.

displacement happens along the y-axis since the phase shift is introduced along v. To avoid the 3 dB increase of the sidelobe level, the slope a (i.e., the slope of the phase over the u-axis or v-axis) must be less than 12 for the array and horn antennas. However, the sidelobe level increase in the case of the patch is much less marked, and even for a greater slope (a =14), it remains under 3 dB.

A more restrictive constraint can be established if it is desired to have a target shift under a given threshold. For

TABLE III
SIDELOBE LEVEL OF THE REFLECTIVITY

	Sidelobe level of the reflectivity [dB]	Slope, a							
		0	2	4	6	8	10	12	14
Patch	x-axis	-14.6	-14.6	-14.6	-14.6	-14.6	-14.5	-14.3	-14.1
	y-axis	-14.7	-14.7	-14.6	-14.3	-14	-13.6	-13	-12.3
Array	x-axis	-14.3	-14.2	-14.1	-14	-13.9	-13.8	-13.7	-13.5
	y-axis	-21.6	-21.6	-21.4	-21	-20.2	-19.6	-18.5	-17
Horn	x-axis	-35.5	-35.6	-35.4	-35.1	-34.6	-34	-33.2	-31.5
	y-axis	-40.2	-39.6	-39.2	-39	-38.9	-38.8	-37.5	-33.9

TABLE IV
SSIM AND PSNR RESULTS. REFERENCE IMAGE FOR SLOPE a =0

		a=2	a=4	a=6	a=8	a=10	a=12	a=14
Patch	SSIM	0.986	0.982	0.983	0.977	0.974	0.972	0.967
	PSNR (dB)	35.98	33.29	32.82	32.44	32.14	31.98	31.72
Array	SSIM	0.990	0.984	0.980	0.975	0.970	0.967	0.932
	PSNR (dB)	36.69	32.61	31.52	31.22	31.02	30.85	30.65
Horn	SSIM	0.995	0.992	0.990	0.988	0.986	0.985	0.984
	PSNR (dB)	35.76	31.06	29.45	29.01	28.91	28.82	28.71

example, to prevent target shifts greater than λ (corresponding λ to the maximum working frequency), the slope a (i.e., the slope of the phase over the u-axis or v-axis), must be kept below 2, as it can be derived from Fig. 8.

Finally, in order to provide a quantitative metric for comparing images, the structural similarity index (SSIM) [27], [28] has been calculated for a grayscale image with respect to a reference image. The closer the SSIM value is to 1, the better the quality of the image.

In this case, the reference image considered is the one corresponding to slope 0. The SSIM of the remaining images is calculated with respect to it.

Likewise, the peak signal-to-noise ratio (PSNR) [29] has been also calculated, and results are included in Table IV. This ratio is used as a quality measurement between the reference image and the reconstructed one. The higher the PSNR, the better the quality of the reconstructed image.

To compute the PSNR, first, it is necessary to calculate the mean-squared error error between the reference image I_{ref} and the image under evaluation I_t as follows:

$$\text{MSE} = \frac{\sum_{M,N}[I_{\text{ref}}(m,n) - I_t(m,n)]^2}{M \cdot N} \tag{9}$$

where M and N are the number of pixels in the input images. Then, the PSNR is calculated using the following equation:

$$\text{PSNR(dB)} = 10\log_{10}\left(\frac{R^2}{\text{MSE}}\right) \tag{10}$$

where R is the maximum of the input image I_{ref}.

As it can be derived from Table IV, the quality of the image worsens as the slope increases, as it was observed in the electromagnetic images, previously displayed.

The linear phase shift across space displaced the target from its original position as a function of the slope of that

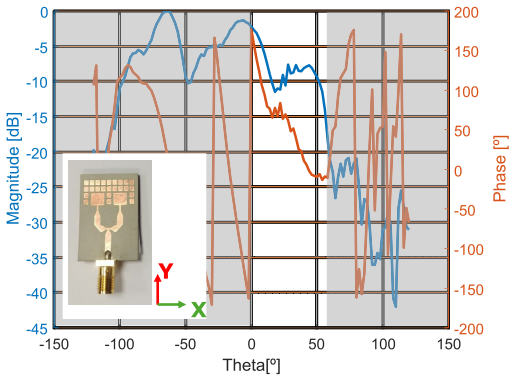

Fig. 9. Radiation pattern cut $\varphi = 90°$ of the array antenna and prototype.

phase shift. In addition, the distortion around it becomes more evident. Nevertheless, the target can be identified and only for applications that need a high accuracy in the target positions (e.g., aligning SAR images and visible images like in [30]), this effect can be harmful.

In order to validate the simulation results on an experimental basis, the real-world radiation pattern of the array antenna has been used in the simulation setup. Specifically, it has been employed the radiation pattern cut $\varphi = 90°$ of the array antenna (see Fig. 9), which corresponds to its E-plane. This has been selected since, as it can be appreciated in Fig. 9, it shows a linear phase offset between $\theta = 0°$ and $\theta = 60°$, with an average slope of -3.23.

The simulation has been repeated; but in this case, the antenna has been moved across the y-axis, with the aim of illuminating the target with the part of the radiation pattern cut corresponding to $\theta = 0°$–$60°$.

The PSF results are shown in Fig. 10. It can be appreciated that the PSF for an ideal radiation pattern is centered, which corresponds to the blue trace. However, when the target is illuminated with the part of the real radiation pattern cut, in which there is a linear phase offset, the PSF moves -11 mm in the y-axis, as it can be observed for the orange trace. Beyond the scope of this work, it is also shows the effect of illuminating the target with the real amplitude and phase distribution of the array radiation pattern cut, which is represented by the yellow trace. It can be observed that, in this case, the PSF suffers further degradation.

As stated above, the average slope of the linear phase is -3.23. Therefore, according to Fig. 8 that shows the displacement of the target as a function of the slope, in the case of the array antenna, the PSF must be displaced λ from its

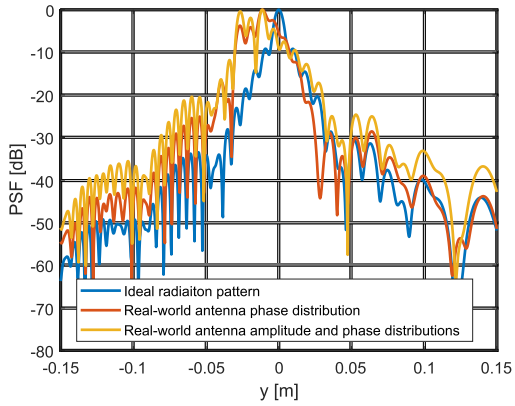

Fig. 10. PSF for the real-world array antenna.

original position. λ at 26 GHz is 11.5 mm, which agrees with the 11 mm of displacement that suffers the orange trace (real phase distribution) with respect to the blue one (ideal radiation pattern). In the case of this type of effect, if there is more than one target in a scenario, it may happen that one of the targets is illuminated by the part of the diagram showing a linear phase offset, and therefore, the target will appear displaced by 1λ from its original position in the electromagnetic image, while the other, which is not affected by the phase offset, will appear in its original position resulting in an erroneous relative position.

B. Linear or Oscillating Phase Shift Across Frequency

In order to model the remaining phase shift along the frequency band once the linear calibration is conducted, a sine function is used, so that the phase term introduced to each frequency (see Fig. 3) can be expressed as follows:

$$\vartheta_m = 2A\sin(\gamma(f_m - f_o)) \tag{11}$$

where A stands for the amplitude of the sine (i.e., the ripple level of the phase), γ represents the angular frequency of the phase shift under analysis (not to be confused with the angular frequency of the signal, $\omega = 2\pi f$), and f_m refers to the actual frequency while f_o refers to the initial frequency. The amplitude of the sine, A, is multiplied by 2 to take into account the round trip in the monostatic setup. The final electromagnetic image is calculated by the linear combination of the images obtained at each frequency according to (5).

In order to understand the impact of the phase oscillation along the bandwidth (which will henceforth be called the ripple level of the phase), it is important to note that the level at each point where the reflectivity is calculated, is multiplied by a factor $\sum_{m=1}^{M} e^{j\vartheta_m}$, being M the number of considered frequencies. Thus, the image amplitude will decay unless the phase shift ϑ_m is the same for all the considered frequencies. To understand this effect, Fig. 11 shows the amplitude of the phase term $\sum_{m=1}^{M} e^{j\vartheta_m}$ for different numbers of cycles and ripple levels of the phase ϑ_m. Isolines joining the points where the amplitude decreases by 3 dB, have been highlighted in red, so that the combination of a number of cycles and ripple level of the phase outside the -3 dB isolines make the amplitude decrease by at least half. It is noticeable that the

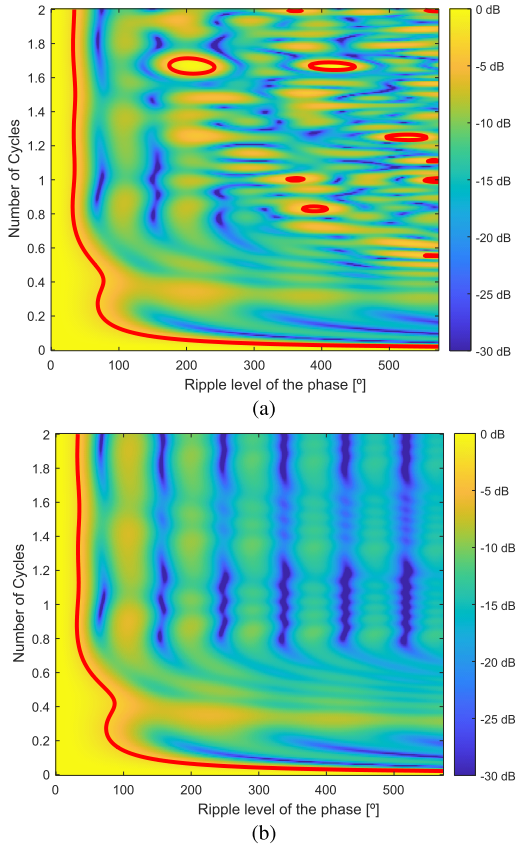

Fig. 11. Dynamic range between number of cycles and signal ripple level. (a) 24.05–24.25 GHz and (b) 22–26 GHz.

tendency of the diagram is similar (taking into account the part under the -3 dB isoline, which is a useful one to avoid image degradation) for both analyzed bandwidths. Hence, the diagram does not depend on the bandwidth under evaluation, as there are no great differences between them.

PSF images for XY cuts of the reflectivity over the plane of the point-like target have been obtained according to (5) and taking into account different number of cycles and ripple level of the phase in order to compare the influence of oscillating shift across frequency.

As the influence of the bandwidth is minimal, the electromagnetic images are only compared for the range of 22–26 GHz frequency band. Fig. 12(a), (d), and (h) presents the electromagnetic images, corresponding to each antenna, obtained for a combination with number of cycles of 1 and ripple level of the phase of 10, so that the point is inside the -3 dB isoline. In addition, Fig. 12(b), (e), and (i) depicted the images for a number of cycles equal to 1 and a ripple level of the phase of 246, so that this combination is outside the -3 dB isoline. Moreover, this last combination of ripple level of the phase and number of cycles has been selected in such a way that the point out of the -3 dB isoline is situated in an area, where the loss of the dynamic range is expected to be high (30 dB). The loss of dynamic range makes noise in the image more noticeable and apparent. Consequently, more artifacts will appear in the image, which will, in general, make the target detection more difficult. Comparing these images two by two, it can be concluded that the dynamic range decays

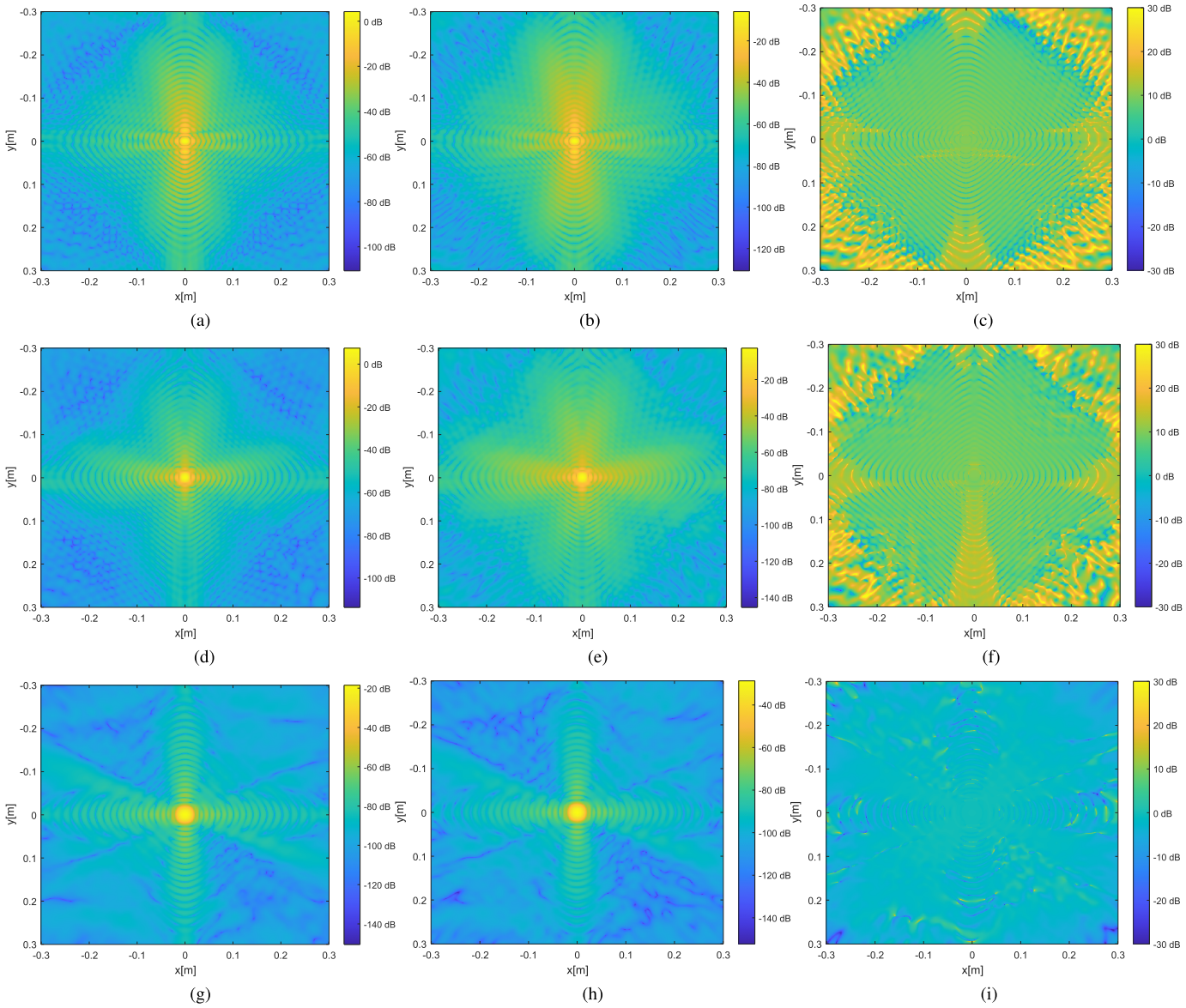

Fig. 12. Electromagnetic images and range comparison. (a) Image for the patch antenna with number of cycles = 1 and level = 10. (b) Image for the patch antenna with number of cycles = 1 and level = 246. (c) Difference between the images obtained with patch antennas. (d) Image for the antenna array with number of cycles = 1 and level = 10. (e) Image for the antenna array with number of cycles = 1 and level = 246. (f) Difference between the images obtained with an antenna array. (g) Image for the horn antenna with number of cycles = 1 and level = 10. (h) Image for the horn antenna with number of cycles = 1 and level = 246. (i) Difference between images corresponding to the use of horn antennas.

by 20 dB, when the combination of the number of cycles and ripple level of the phase is outside the −3 dB isoline. This result is in line with the relevant expected dynamic range loss. It should be noticed that a different scale is used to represent the results obtained with a point inside and outside the −3 dB isoline, but keeping the 120 dB of range, in order to emphasize that the main difference between the two images is the loss of dynamic range. Finally, the subtraction of each pair of images (obtained for a point inside and outside the −3 dB isoline) are exhibited in Fig. 12(c), (f), and (i), respectively, for each antenna. It can be concluded that the combination of a number of cycles and ripple level of the phase outside the −3 dB isoline degrades the image; however, the target can be distinguished in all cases but at the expense of a reduced dynamic range for lateral reflectivity images. Nevertheless, the quality of these images is not compromised if the ripple level of the phase is kept below 60°, as long as the oscillation is moderate (<0.5 cycles). Moreover, if the ripple level is below 40°, the oscillation does not have a relevant impact.

TABLE V
SSIM AND PSNR RESULTS FOR EACH PAIR OF IMAGES (WITH NUMBER OF CYCLES = 1 AND LEVEL = 10 WHICH IS THE REFERENCE IMAGE AND WITH NUMBER OF CYCLES = 1 AND LEVEL = 246)

	SSIM	PSNR (dB)
Patch	0.917	34.13
Array	0.944	34.32
Horn	0.998	53.17

The SSIM and PSNR have been calculated (see Table V) for each pair of images [Fig. 12(a) and (b), (d) and (e), and (g) and (h)]. From the result, it can be concluded that the

TABLE VI
MAXIMUM VALUE OF THE PSF FOR EACH COMBINATION OF *n*CYCLES AND *A*

	LC	nCycles=0	nCycles=0.5			nCycles=1			nCycles=2		
		A=0	*A*=0	*A*=0.1	*A*=0.2	*A*=0	*A*=0.1	*A*=0.2	*A*=0	*A*=0.1	*A*=0.2
Patch	x-axis	1	1	0.94	0.81	1	0.78	0.26	1	0.77	0.25
	y-axis	1	1	0.94	0.81	1	0.78	0.28	1	0.77	0.25
	z-axis	1	1	0.94	0.81	1	0.80	0.36	1	0.78	0.28
Array	x-axis	1	1	0.94	0.79	1	0.77	0.25	1	0.77	0.25
	y-axis	1	1	0.94	0.79	1	0.78	0.27	1	0.77	0.25
	z-axis	1	1	0.94	0.79	1	0.82	0.41	1	0.78	0.29
Horn	x-axis	1	1	0.94	0.77	1	0.72	0.13	1	0.72	0.13
	y-axis	1	1	0.94	0.77	1	0.72	0.13	1	0.72	0.13
	z-axis	1	1	0.93	0.77	1	0.80	0.37	1	0.74	0.22

image quality is slightly deteriorated, when the point is outside the −3 dB isoline. It has been observed that the decrease in the image quality is greater for omnidirectional antennas, since the results show that the array antenna has slightly worse results and the patch even lower than the horn antenna. Thus, the effect is less evident in the case of high directivity antennas, as it can be derived from the SSIM and PSNR results.

The linear or oscillating phase shift across frequency degrades the electromagnetic images in terms of dynamic range. However, the target can be clearly identified in the most unfavorable cases (point outside the −3 dB isoline). Furthermore, the dynamic range loss is smaller for high-directivity antennas.

C. Phase Center Shift Across the Bandwidth

The last effect under evaluation is related to the displacement of the phase center of the antennas across the bandwidth. In a similar fashion to Section II-B, the possible displacements of the phase center along the z-axis will be modeled according to

$$z_m = A\sin(\gamma(f_m - f_0)) \tag{12}$$

where A refers to the amplitude of the function (i.e., the ripple of the phase center displacement along the height axis), in a similar fashion to the previous case, γ represents the angular frequency of the phase center under analysis (not to be confused with the angular frequency of the signal, $\omega = 2\pi f$), while f_m represents the actual frequency and f_0 the initial one.

It should be noted that, as previously mentioned, some studies [14], [15] have analyzed the effects of incorrect antenna positioning on electromagnetic imaging, showing that moderate lateral displacements in the x- and y-axis have practically no impact, which motivates us to study only the displacement along the z-axis. The phase center shift is equivalent to the incorrect positioning of the antenna since the electromagnetic waves do not emanate from the same point. For this reason, in this work, it is modeled by applying the offset z_m to the position, where the radiation pattern emanates. After that, the image is generated according to the algorithm in (3).

Fig. 13 depicts the amplitude of the PSF at the center of the target for different number of cycles in the bandwidth under analysis (22–26 GHz) versus the ripple of the phase center displacement. It can be appreciated that there is a narrow part where the image will not experiment degradation, which

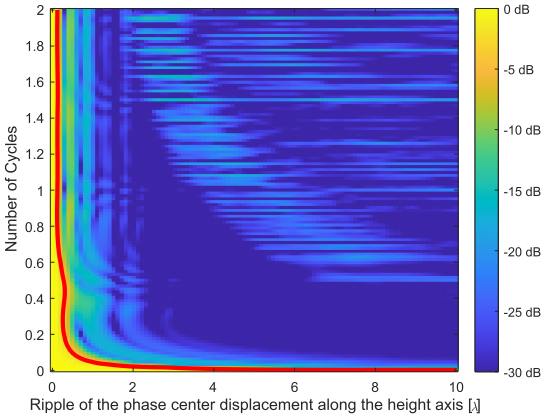

Fig. 13. Amplitude of the PSF at the center of the target in case of displacing the phase center for different combinations of the number of cycles and ripple of the phase center displacement.

corresponds to the yellow area under the −3 dB isoline that has been plotted in red again. Hence, the combination of a number of cycles and ripple of the phase center displacement outside the −3 dB isolines makes the amplitude decrease by at least half. In this case, the number of cycles is not relevant as long as the ripple of the phase center displacement is under 0.1λ. Otherwise, the image quickly degrades even for slow oscillations of the phase center.

Electromagnetic images for all the antennas evaluated in this work have been obtained taking into account different combinations of number of cycles and ripple of the phase center displacement along the z-axis. For comparison purposes, the linear cut (LCs) of the PSF under analysis have been obtained, which are depicted in Fig. 14. For each image, the cuts have been normalized with respect to the the maximum amplitude of the PSF, which is achieved if no phase center displacements are considered. Analyzing the LCs along the x- and y-axis, which correspond to Fig. 14(a) and (b) for the patch antenna, Fig. 14(d) and (e) in the case of the array antenna, and Fig. 14(g) and (h) for the horn antenna, it can be concluded that the ripple of the phase center displacement has a great influence on the quality of the images obtained since, with a ripple level higher than 0.1λ, the image quality worsens significantly. However, the number of cycles has practically no influence on the results as long as the ripple of the phase center displacement is under that threshold.

In the case of the LC through the z-axis, which are shown in Fig. 14(c) in the case of the patch antenna, Fig. 14(f) for

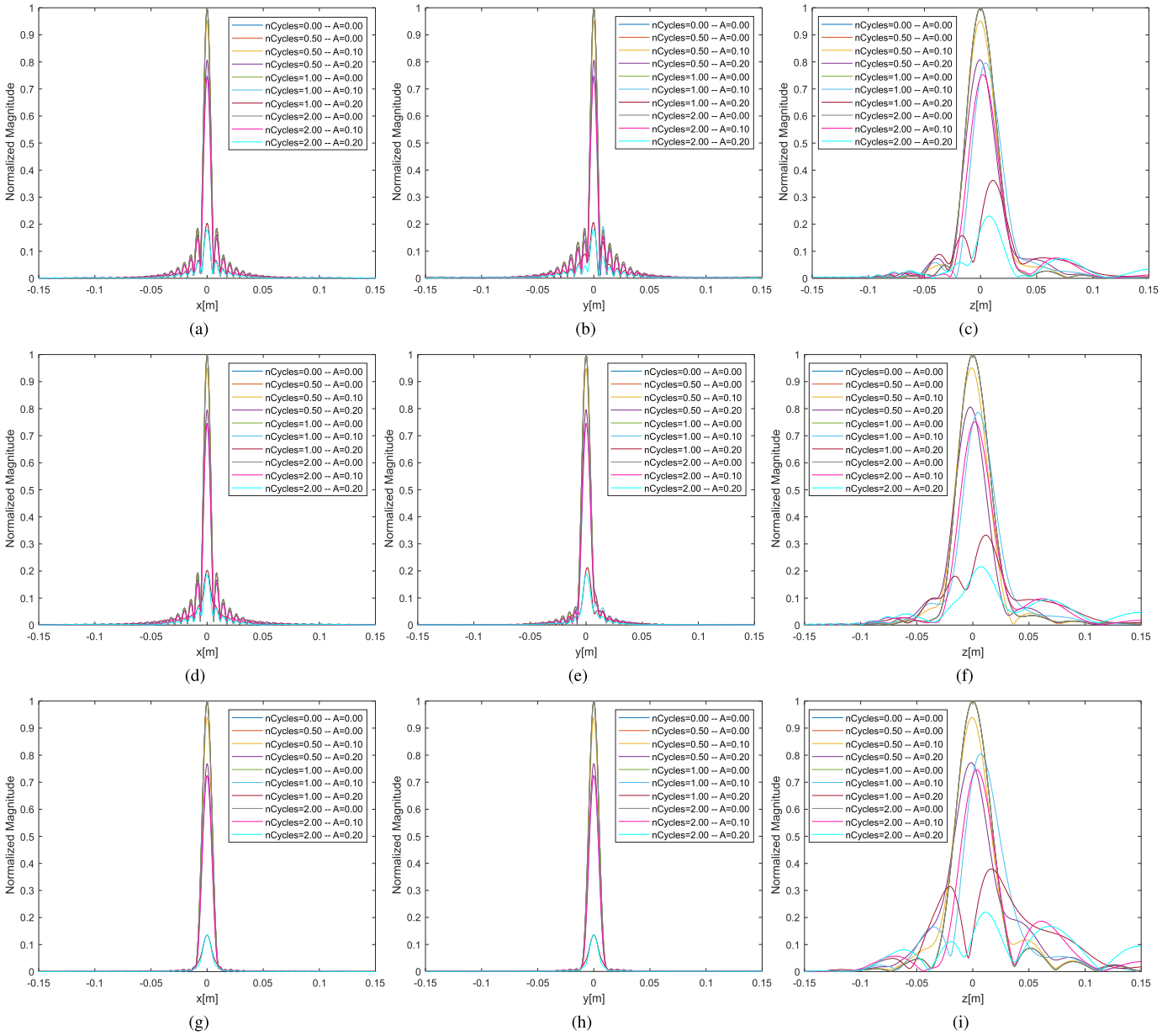

Fig. 14. LCs of the PSF for each antenna. (a) LC through the x-axis for patch antenna, (b) LC through the y-axis for patch antenna, (c) LC through the z-axis for patch antenna, (d) LC through the x-axis for array antenna, (e) LC through the y-axis for array antenna, (f) LC through the z-axis for array antenna, (g) LC through the x-axis for horn antenna, (h) LC through the y-axis for horn antenna, and (i) LC through the z-axis for horn antenna.

the array antenna, and Fig. 14(i) for the horn, the conclusions reached are in agreement with those of the previous case. If the ripple of the phase center displacement exceeds the threshold of 0.1λ, then the image quality degradation is significant, while the number of cycles has a much smaller influence on it.

In order to quantitatively compare the results, the maximum value of the PSF for each LC and combination of a number of cycles and A, is given in Table VI. The same conclusions are extracted from it. As the ripple of the phase center displacement increases, the quality of the image degrades. It is noteworthy that the loss of dynamic range is slightly less in the case of the z-axis.

Therefore, it has been concluded that the quality of the images can be significantly worsen if the threshold established is not met, as the images are rapidly degraded even for slow oscillations of the phase center.

IV. Conclusion

In this work, the influence of the nonuniform phase of the antenna radiation pattern and the effect of this feature on SAR have been investigated.

It has been shown that the phase plays a fundamental role in the quality of the images obtained, since the imaging algorithms assume an ideal spherical wavefront at every frequency. Understanding the effects of phase shifts on electromagnetic images is essential to check if an antenna will have a good performance for electromagnetic imaging.

It has been demonstrated that phase shift throughout space can result in a displacement of the target from its original

position that is directly proportional to the slope of the linear phase shift. In this case, the value of the slope a must remain below 2 to avoid target displacements larger than λ. Likewise, if target shifting is not critical, to avoid an increase of more than 3 dB in the reflectivity sidelobe level, the slope a must be less than 12.

The oscillating shift along the frequency as a consequence of a not perfect calibration causes the dynamic range of lateral images. Large phase shifts with frequency should be avoided. In this case, although the target can be identified always, it is desirable not to exceed a ripple level of 60° as long as the number of cycles remains below 0.5, so that the dynamic range loss is negligible. Nevertheless, if high oscillation is considered (up to 2 number of cycles), a good quality images can be obtained if the signal ripple is kept under 40°.

Finally, the displacement of the phase center of the antenna also plays a crucial role, causing a decrease in the image quality for a ripple level greater than 0.1λ in the height direction. In this case, the number of cycles has practically no influence.

If some of these effects occur simultaneously, it would be expected to observe several of their impacts in the resulting images. Finally, it is relevant to note that the previous analysis was performed assuming monostatic conditions for the acquisition. However, similar conclusions are expected for multistatic setups as the phase compensation algorithms have similar mechanisms.

REFERENCES

[1] I. M. Skolnik, *Introduction to RADAR Systems*. New York, NY, USA: McGraw-Hill, 1980.

[2] M. Soumekh, *Synthetic Aperture Radar Signal Processing With MATLAB Algorithms*. Hoboken, NJ, USA: Wiley, 1999.

[3] V. K. Kukkala, J. Tunnell, S. Pasricha, and T. Bradley, "Advanced driver-assistance systems: A path toward autonomous vehicles," *IEEE Consum. Electron. Mag.*, vol. 7, no. 5, pp. 18–25, Sep. 2018, doi: 10.1109/MCE.2018.2828440.

[4] A. Haryono, M. S. U. Rahman, and M. Abou-Khousa, "Inspection of non-metallic pipes using microwave non-destructive testing (NDT)," in *Proc. IEEE Int. RF Microwave Conf. (RFM)*, Dec. 2018, pp. 219–222, doi: 10.1109/RFM.2018.8846531.

[5] J. R. Gallion and R. Zoughi, "Millimeter-wave imaging of surface-breaking cracks in steel with severe surface corrosion," *IEEE Trans. Instrum. Meas.*, vol. 66, no. 10, pp. 2789–2791, Oct. 2017, doi: 10.1109/TIM.2017.2735658.

[6] T.-H. Pham, K.-H. Kim, and I.-P. Hong, "A study on millimeter wave SAR imaging for non-destructive testing of rebar in reinforced concrete," *Sensors*, vol. 22, no. 20, p. 8030, Oct. 2022.

[7] M. ELsaadouny, J. Barowski, J. Jebramcik, and I. Rolfes, "Millimeter wave SAR imaging for the non-destructive testing of 3D-printed samples," in *Proc. Int. Conf. Electromagn. Adv. Appl. (ICEAA)*, Granada, Spain, Sep. 2019, pp. 1283–1285, doi: 10.1109/ICEAA.2019.8879272.

[8] S. Li and S. Wu, "Low-cost millimeter wave frequency scanning based synthesis aperture imaging system for concealed weapon detection," *IEEE Trans. Microwave Theory Techn.*, vol. 70, no. 7, pp. 3688–3699, Jul. 2022.

[9] A. A. Farsaei, F. Mokhtari-Koushyar, S. M. J. Seyed-Talebi, Z. Kavehvash, and M. Shabany, "Improved two-dimensional millimeter-wave imaging for concealed weapon detection through partial Fourier sampling," *J. Infr., Millim., Terahertz Waves*, vol. 37, no. 3, pp. 267–280, Mar. 2016, doi: 10.1007/s10762-015-0223-z.

[10] M. T. Bevacqua, S. Di Meo, L. Crocco, T. Isernia, and M. Pasian, "Millimeter-waves breast cancer imaging via inverse scattering techniques," *IEEE J. Electromagn., RF Microwave Med. Biol.*, vol. 5, no. 3, pp. 246–253, Sep. 2021.

[11] G. Yuan and R. Zoughi, "Millimeter wave reflectometry and imaging for noninvasive diagnosis of skin burn injuries," *IEEE Trans. Instrum. Meas.*, vol. 66, no. 1, pp. 77–84, Jan. 2017.

[12] D. M. Sheen, D. L. Mcmakin, and T. E. Hall, "Three-dimensional millimeter-wave imaging for concealed weapon detection," *IEEE Trans. Microwave Theory Techn.*, vol. 49, no. 9, pp. 1581–1592, Sep. 2001.

[13] J. M. Lopez-Sahcnez and J. Fortuny-Guasch, "3-D radar imaging using range migration techniques," *IEEE Trans. Antennas Propag.*, vol. 48, no. 5, pp. 728–737, May 2000, doi: 10.1109/8.855491.

[14] Y. Gao, M. T. Ghasr, and R. Zoughi, "Effects of and compensation for translational position error in microwave synthetic aperture radar imaging systems," *IEEE Trans. Instrum. Meas.*, vol. 69, no. 4, pp. 1205–1212, Apr. 2020.

[15] Y. Gao, M. T. Ghasr, and R. Zoughi, "Effects of translational position error on microwave synthetic aperture radar (SAR) imaging systems," in *Proc. IEEE Int. Instrum. Meas. Technol. Conf.*, May 2018, pp. 1–6.

[16] M. Horst, M. T. Ghasr, and R. Zoughi, "Effect of instrument frequency uncertainty on wideband microwave synthetic aperture radar (SAR) images," in *Proc. IEEE Int. Instrum. Meas. Technol. Conf.*, May 2017, pp. 1–5, doi: 10.1109/I2MTC.2017.7969806.

[17] M. J. Horst, M. T. Ghasr, and R. Zoughi, "Effect of instrument frequency uncertainty on wideband microwave synthetic aperture radar images," *IEEE Trans. Instrum. Meas.*, vol. 68, no. 1, pp. 151–159, Jan. 2019, doi: 10.1109/TIM.2018.2834098.

[18] C. Liu, M. T. A. Qaseer, and R. Zoughi, "Influence of antenna pattern on synthetic aperture radar resolution for NDE applications," *IEEE Trans. Instrum. Meas.*, vol. 70, pp. 1–11, 2021.

[19] Y. Á. López and F. Las-Heras, "On the use of an equivalent currents-based technique to improve electromagnetic imaging," *IEEE Trans. Instrum. Meas.*, vol. 71, pp. 1–13, 2022, doi: 10.1109/TIM.2022.3181926.

[20] Y. Á. López, J. Laviada, A. Arboleya, and F. Las-Heras, "A backpropagation imaging technique for subsampled synthetic apertures," *IEEE Trans. Instrum. Meas.*, vol. 72, pp. 1–16, 2023, doi: 10.1109/TIM.2023.3244843.

[21] A. F. Berdasco, J. Laviada, M. E. de Cos Gómez, and F. Las-Heras Andrés, "Performance analysis of mm-wave wearable antennas for visually impaired aid," in *Proc. 17th Eur. Conf. Antennas Propag.*, Berd, Italy, Mar. 2023, pp. 1–5, doi: 10.23919/EuCAP57121.2023.10133568.

[22] A. Zhuravlev, V. Razevig, A. Rogozin, and M. Chizh, "Microwave imaging of concealed objects with linear antenna array and optical tracking of the target for high-performance security screening systems," *IEEE Trans. Microwave Theory Techn.*, vol. 71, no. 3, pp. 1326–1336, Mar. 2023.

[23] *3D High Frequency Simulation Software*. Accessed: Dec. 5, 2023. [Online]. Available: https://www.ansys.com/products/electronics/ansys-hfss

[24] A. F. Berdasco, M. E. de Cos Gómez, H. F. Álvarez, and F. L. Andrés, "Array antenna with HIS metasurface for mmWave imaging applications," in *Proc. 16th Eur. Conf. Antennas Propag. (EuCAP)*, Mar. 2022, pp. 1–5, doi: 10.23919/EuCAP53622.2022.9769433.

[25] A. Flórez Berdasco, M. E. de Cos Gómez, H. Fernández Álvarez, and F. Las-Heras, "Millimeter wave array-HIS antenna for imaging applications," *Appl. Phys. A*, vol. 129, no. 6, p. 397, Jun. 2023, doi: 10.1007/s00339-023-06676-0.

[26] A. F. Berdasco, J. Laviada, M. E. de Cos Gomez, and F. Las-Heras, Jan. 23, 2024, "Radiation pattern of patch and array-HIS antennas obtained with HFSS," *IEEE Dataport*, Jan. 23, 2024, doi: 10.21227/hfsv-dv39.

[27] (2024). *Structural Similarity (SSIM) Index for Measuring Image Quality—MATLAB*. [Online]. Available: https://www.mathworks.com/help/images/ref/ssim.html

[28] H. Ming Yao, H. Huan Zhang, L. Jiang, and M. Kwok Po Ng, "Fast electromagnetic inversion solver based on conditional generative adversarial network for high-contrast and heterogeneous scatterers," *IEEE Trans. Antennas Propag.*, vol. 72, no. 4, pp. 3485–3494, Apr. 2024.

[29] Y. Peng, Z. Sheng, and G. He, "Near-field low-storage SAR imaging with spatio-temporal sub-nyquist samples," *IEEE Sensors J.*, vols. SEN-24, no. 12, pp. 19442–19453, Aug. 1109, doi: 10.1109/JSEN.2024.3393761.

[30] J. Laviada, A. Arboleya-Arboleya, Y. Álvarez, B. González-Valdés, and F. Las-Heras, "Multiview three-dimensional reconstruction by millimetre-wave portable camera," *Sci. Rep.*, vol. 7, no. 1, p. 6479, Jul. 2017, doi: 10.1038/s41598-017-06475-7.

Alicia Flórez Berdasco (Graduate Student Member, IEEE) was born in Cangas del Narcea, Asturias, Spain. She received the B.Sc. and M.Sc. degrees in telecommunication engineering from the University of Oviedo, Gijón, Spain, in 2019 and 2021, respectively, where she is currently pursuing the Ph.D. degree, with the support of an FPI Grant from the Spanish Government.

Her research interests concern the design and characterization of antennas and metasurfaces for wearable systems with applications in RFID, 5G, the Internet of Things (IoT) and radar, and the electromagnetic characterization of the novel involved materials.

Jaime Laviada was born in Gijón, Spain. He received the M.S. degree in telecommunication engineering and the Ph.D. degree from the Universidad de Oviedo, Gijón, in 2005 and 2010, respectively.

In 2006, he joined the Research Group Signal Theory and Communications, Universidad de Oviedo, where he has been involved in multiple national and European projects as well as contracts with several companies. In 2015, he moved to the Antennas Group, Universidad Publica de Navarra, Pamplona, Spain, with a National Postdoctoral Fellowship collaborating on several applied research projects. Finally, he moved back to the Universidad de Oviedo, where he currently holds the position of an Associate Professor. In addition, he was a Visiting Scholar with the Electromagnetics and Communications Laboratory, The Pennsylvania State University, State College, USA, from 2007 to 2008, and also with the Applied Microwave Nondestructive Testing Laboratory, Missouri University of Science and Technology, Rolla, MO, USA, in 2017. His research interests include numerical techniques applied to electromagnetic (EM) imaging, antenna measurements, method of moments, and antenna pattern synthesis.

María Elena de Cos Gómez (Member, IEEE) received the degree in telecommunication engineering and the Ph.D. degree from the University of Cantabria, Santander, Spain, in 2002 and 2006, respectively.

She was a Researcher Engineer in collaboration with ACORDE S.A., Santander, from 2004 to 2007. In 2007, she joined the Area de Teoria de la Senal y Comunicaciones, Universidad de Oviedo, Gijón, Spain. She has authored or co-authored over 75 journals and conference contributions. Her current research interests include metamaterials design and its applications to antennas and microwave circuits, the design of antennas for wearable and RFID systems, radar cross-section (RCS) reduction, location techniques, and wireless sensor network design and applications.

Dr. de Cos Gómez was awarded as an Outstanding IEEE AWPL Reviewer from 2017 to 2018. She has been an Associate Editor of the IEEE ANTENNAS AND WIRELESS PROPAGATION LETTERS since 2018.

Fernando Las-Heras (Senior Member, IEEE) received the M.S. and Ph.D. degrees in telecommunication engineering from the Technical University of Madrid (UPM), Madrid, Spain, in 1987 and 1990, respectively.

From 1988 to 1990, he was a National Graduate Research Fellow with UPM, where he was an Associate Professor with the Department of Signal, Systems, and Radiocommunications, from 1991 to 2000. Since December 2003, he has been a Full Professor with the University of Oviedo, Gijón, Spain, where he was a Vice Dean of telecommunication engineering with the Technical School of Engineering from 2004 to 2008. He was a Visiting Lecturer with the National University of Engineering, Lima, Peru, in 1996; a Visiting Researcher with Syracuse University, Syracuse, NY, USA, in 2000; and a short-term Visiting Lecturer with ESIGELEC, Saint-Étiennedu-Rouvray, France, from 2005 to 2011. He has been the Head of the Research Group Signal Theory and Communications TSC-UNIOVI, Department of Electrical Engineering, University of Oviedo, since 2001. He has led and participated in a great number of research projects and has authored over 230 articles published in indexed scientific journals on topics of antennas, propagation, metamaterials, and inverse problems with application to antenna measurement, electromagnetic (EM) imaging, and localization, developing computational EMs algorithms and technology on microwaves, millimeter wave, and terahertz (THz) frequency bands.

Dr. Las-Heras was a member of the Board of Directors of the IEEE Spain Section from 2012 to 2015; a member from 2016 to 2017 and a Vice-President from 2020 to 2022 of the Board of the Joint IEEE Microwave Theory and Techniques Society (MTT-S) and Antennas and Propagation Society (AP-S) Spain Chapter; a member of the Science, Technology and Innovation Council of Asturias from 2010 to 2012; and a President of the Professional Association of Telecommunication Engineers, Asturias, Spain. He was the Telefónica Chair of "RF Technologies," "Information and Communications Technologies (ICTs) applied to Environment," and "ICTs and Smartcities" with the University of Oviedo, from 2005 to 2015.